Inkjet printing P(VDF-TrFE-CTFE) actuators for large bending strains

Sekar, S.A.; Hunt, A.

Important note
To cite this publication, please use the final published version (if applicable).
Please check the document version above.

PAPER • OPEN ACCESS

Inkjet printing P(VDF-TrFE-CTFE) actuators for large bending strains

View the article online for updates and enhancements.

You may also like

Inkjet printing P(VDF-TrFE-CTFE) actuators for large bending strains

S A Sekar ⓘ and A Hunt* ⓘ

Department of Precision and Microsystems Engineering Faculty of Mechanical Engineering (ME), Delft University of Technology, Mekelweg 2, Delft 2628CD, The Netherlands

E-mail: a.hunt@tudelft.nl

CrossMark

Abstract

Additive manufacturing of sensors and actuators together with structural materials and electronics will make it possible to fabricate innovative system designs that are overly laborious to realise with conventional methods. While printing of the structural materials and electronics are advancing fast, the additive manufacturing methods for actuators and sensors are in an earlier stage of development. This research will develop a manufacturing process for entirely inkjet printed electroactive polymer (EAP) actuators basing on the P(VDF-TrFE-CTFE) relaxor ferroelectric polymer and Ag electrodes. The process consists of (1) printing an Ag layer on a polyethylene terephthalate (PET) substrate for the bottom electrode; (2) formulating, printing and annealing a P(VDF-TrFE-CTFE) ink for the EAP layer; and (3) printing and sintering an Ag layer on the plasma-treated EAP surface to form the top electrode. Two actuator variations, addressed as *DMC* and *KM512*, are manufactured and characterised by their: (a) response to quasi-static excitation (1 Hz sine wave); (b) hysteresis behaviour; (c) actuation amplitude variation with the input voltage; and (d) frequency response. The 18 mm long actuators showed 91.4 μm (*DMC*, 200 V_{pp}) and 224 μm (*KM512*, 275 V_{pp}) deflections in response to 1 Hz sinusoidal excitation, and 1.10 mm (*DMC*, 113 Hz, 200 V_{pp}) and 1.72 mm (*KM512*, 114 Hz, 200 V_{pp}) deflections in resonant operation. It is 55% more quasi-static strain and 470% more resonant strain than in earlier fully inkjet-printed polyvinylidene fluoride (PVDF) -based actuators, and comparable to similar partially inkjet-printed actuators. This is the first time that inkjet printing of all three layers of a relaxor ferroelectric actuator have been achieved.

Supplementary material for this article is available online

1. Introduction

Additive manufacturing of passive material structures has significantly matured over the past decade, and in the meantime the printing of electronics has been gaining momentum [1–3].

Complementing these methods with printing of sensors and actuators will enable fast and cost-effective means to fabricate innovative mechatronics solutions, e.g. solid-state positioning systems and robots, lab-on-a-chip devices, adaptive optics components and vibration suppressors for the high-tech engineering domain. In contrast, printing of smart material sensors and actuators is in a much earlier stage of development [4–6]. A likely method to accommodate printing of such transducers is inkjet printing (IJP)—a contactless fabrication method that can construct objects via incrementally depositing thin material layers ($<10\,\mu$m) of required geometry, drop by drop [7]. IJP is increasingly widely used to print structural

materials with a wide variety of properties [8, 9], and it is the primary method for printing electronics [1, 10]. While IJP of functional materials poses many challenges [11], advances in printing conductive tracks on flexible substrates [12] has also enabled printing wire-based electromagnetic [13] and electrothermal [14] actuators. Printing electroactive polymer (EAP) transducers poses additional challenges due to the need for additional materials and interfaces: formulating rheologically feasible EAP (and electrode) inks, achieving layer adhesion and curing of the inks, and assuring that the successive manufacturing steps do not damage the previously manufactured structures [1, 11, 15].

A number of advances have been reported in IJP to fabricate parts of EAP sensors and actuators, while only few have printed the entire transducer. Poly(3,4-ethylenedioxythiophene) polystyrene sulfonate (PEDOT:PSS) has been printed on PVDF [16, 17] and interpenetrating polymer network [18] membranes to produce ionic EAP actuators; on PVDF to make piezoelectric bimorph actuator components [19]; and on P(VDF-TrFE) to make piezoelectric sensors [20]. Inks and processes for IJP EAP have been developed for P(VDF-TrFE) in [21], and for both P(VDF-TrFE) and P(VDF-TrFE-CTFE) in [22], whereas the latter study further used sputtering to deposit Au electrodes to produce force sensors. Banquart *et al* reported IJP a P(VDF-TrFE) layer on a silicon substrate and sputter-coating the top electrode to form ultrasound transducers [23], and Abdolmaleki *et al* combined IJP of P(VDF-TrFE)–AGO nanocomposites with painting Ag electrodes to form biomedical monitoring sensors [24]. P(VDF-TrFE)-based transducers with IJP'ed Ag electrodes were reported by Alique *et al* [25], and P(VDF-TrFE-CTFE)-based actuators with IJP'ed carbon black electrodes were reported in [26, 27], whereas the EAP layers in these studies were respectively screen-printed and spincoated. IJP'ing both the P(VDF-TrFE) EAP and the top electrode (Ag) on an Ag-coated polycarbonate substrate was reported in [28], resulting in EAP actuators. IJP'ing the EAP layer and both the electrodes has been reported in very few studies: Pabst *et al* used P(VDF-TrFE) and Ag inks to print piezoelectric polymer actuators on a PET substrate [29]; and Thuau *et al* printed P(VDF-TrFE) and Ag inks on a polyethylene naphthalate (PEN) substrate, and studied the resulting transducers in pressure sensing and actuation response measurements [7].

Therefore, IJP the entire EAP transducer has been achieved only for the P(VDF-TrFE) (EAP) and Ag (electrodes) combination [7, 29]. While the P(VDF-TrFE) is well-suited for sensing purposes due to the strong piezoelectric response [21] and high sensitivity (e.g. 74 pCN^{-1} [30]), the attainable material strains in actuation are low (e.g. from 0.15% [31] up to 0.7% [32] depending on the processing). The P(VDF-TrFE-CTFE) terpolymer is a relaxor ferroelectric that exhibits strong electrostrictive behaviour [33] and high material strains (e.g. 5% [34]), making it more versatile for actuation.

This paper develops a process for IJP P(VDF-TrFE-CTFE)-based bending EAP transducers. The actuator construction bases on a bending unimorph cantilever concept (see figure 1).
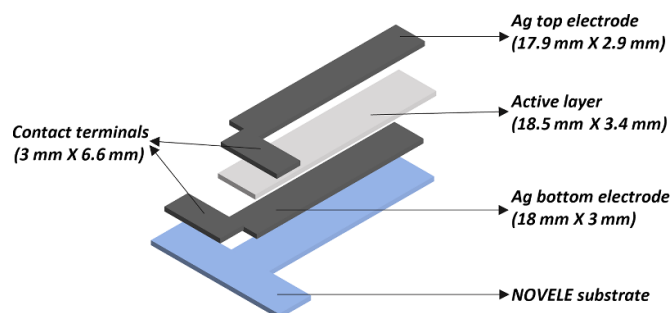

Figure 1. Actuator design and construction.

The individual steps of incrementally printing the bottom electrode, the EAP layer and the top electrode on a PET-based substrate are addressed in sections 2.1–2.4. Composition of the resulting actuators are studied according to sections 2.5 and 2.6 explains their performance characterisation. The results are reported and discussed respectively in sections 3–5 concludes this paper.

2. Materials and methods

Actuator manufacture bases on the design shown in figure 1, and consists of consecutive steps of printing and pre/post-treatments, as graphically explained in figure 2. The process starts with printing the bottom electrode on a PET substrate with micro-porous resin coating (NovaCentrix Novele IJ-220) [35] using an Ag nanoparticle ink (Mitsubishi NBSIJMU01) [36], as explained in section 2.1. Next, basing on the P(VDF-TrFE-CTFE) relaxor ferroelectric polymer (Arkema Piezotech RT-TS) [34], the EAP inks are formulated for rheological compatibility with the DMC and KM512 printheads, as described in section 2.2. These inks are then used to print and cure the EAP layer, as explained in section 2.3. Next, the polymer surface is modified in oxygen plasma, the top electrode is printed from an Ag nanoparticle ink (NovaCentrix JS-A211) [37] and then cured, as described in section 2.4. Morphology and performance of the resulting actuators are respectively studied according to the sections 2.5 and 2.6.

The printing processes are implemented on a Pixdro LP50 system that can operate multiple types of industrial printheads. It allows up to 500 mm s^{-1} print speeds, up to 90 °C printbed temperatures, and integrated UV curing [38]. The printing steps are performed on three disposable Dimatix DMC-11610 printheads (16 nozzles in a single row, 21.5 μm orifice size, 254 μm nozzle pitch, 10 pl droplet volume) [39], and one Konica Minolta KM512 printhead (512 nozzles in two rows, 70.5 μm nozzle pitch, 14 pl droplet volume) [40]. Both printheads base on the drop-on-position printing concept [41] and allow heating their nozzles up to 60 °C.

2.1. Bottom electrode fabrication

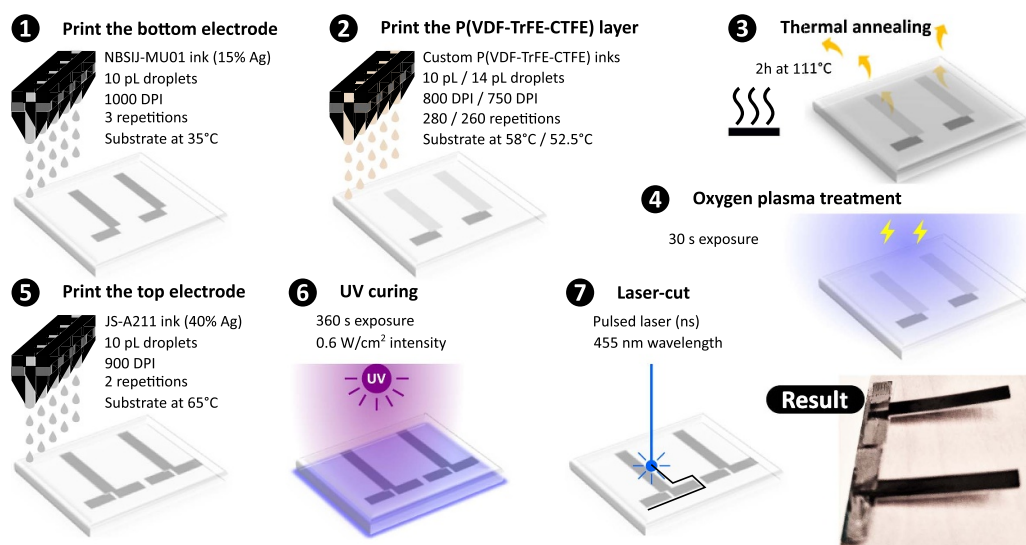The bottom electrode is printed on the NovaCentrix Novele IJ-220 substrate [35] using the Pixdro LP50 system and a

Figure 2. The fabrication process for fully inkjet printing relaxor ferroelectric actuators.

Dimatix DMC-11610 printhead loaded with the Mitsubishi NBSIJMU01 Ag nanoparticle ink. The IJ-220 substrate is a 140 μm thick PEN sheet (glass transition temperature 120 °C) with a micro-porous resin coating to facilitate ink adhesion. The bottom electrode is printed from the Mitsubishi NBSIJMU01 nanoparticle dispersion ink with 15 wt.% Ag content [36]. The ink self-sinters when printed on the micro-porous substrate surface, attaining high conductivity without any post-processing. Alternatively, the bottom electrode could be printed from a multitude of other conductive inks (e.g. metal-, polymer- or carbon-based) [1], whereas this would introduce the need for additional steps of substrate preparation and post-processing.

Before loading the NBSIJMU01 ink into the printhead reservoir, it is filtered using a 0.45 μm polytetrafluoroethylene (PTFE) filter. This prevents clogging of the nozzles by the larger Ag particles that may have agglomerated since the ink was manufactured. The printing settings (see table 1) are established experimentally, and figure 3(a) depicts the eventual jetting waveform that was used for printing the bottom electrode. It results in a consistent formation of *ca* 10 pl droplets at 6 m s^{-1} velocity, and no formation of satellite droplets. A 1000 DPI printing resolution is obtained by using a 1350 Hz firing rate at 80 mm s^{-1} printing speed. For a homogeneous conducting electrode, three printing iterations are required. During the printing the substrate table is maintained at 35 °C to speed up the solvent evaporation, eliminate the coffee ring effects [42] and maintain consistent printing temperature from day to day. Once printed on the IJ-220 substrate, the Ag ink turns from a dark brown liquid into a glossy silver film.

2.2. EAP ink formulation

To attain high actuation strains, this study employs the P(VDF-TrFE-CTFE) terpolymer that exhibits a strong electrostrictive response and produces material strains of up to 5% [34]. For printability, the EAP inks must fulfil specific criteria on

Table 1. Printing settings and ink properties in the electrode deposition steps.

Specification	Bottom electrode	Top electrode
Ag content (wt.%)	15	40
Z number	9.45	2.92
Print repetitions	3	2
Resolution (DPI)	1000	900
Print speed (mm s^{-1})	80	50
Drop spacing (μm)	ca 25	ca 28
Post-processing	*None*	*UV sintering*
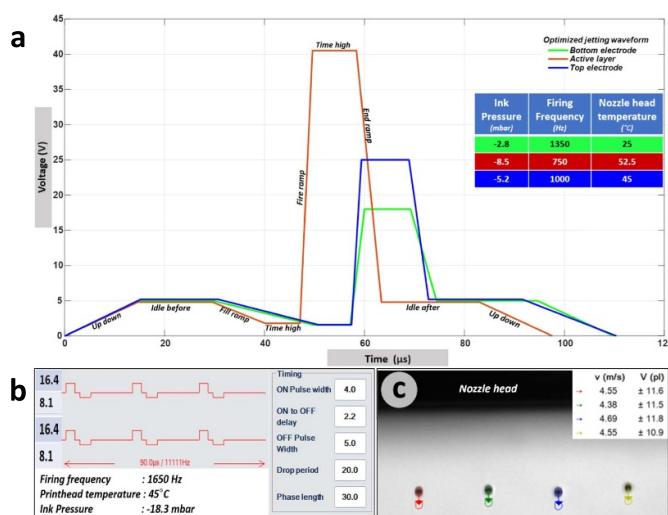
Figure 3. Jetting the ink droplets: (a) waveforms for jetting the conductive and EAP inks on the Dimatix DMC-11610 printhead; (b) waveform for jetting the EAP ink on the Konica Minolta KM512 printhead; and (c) analysing the EAP ink jetting in the DropView software module (Pixdro LP50).

their rheological properties, as explained in section 2.2.1. Basing on this, the EAP inks are formulated by dissolving the P(VDF-TrFE-CTFE) polymer in a combination of methyl

ethyl ketone (MEK) and dimethyl sulphoxide (DMSO) solvents, as explained in section 2.2.2. Since the the rheological requirements depend on the nozzle properties, separate inks are formulated for the DMC and KM512 printheads.

2.2.1. Rheological requirements. In order to ensure a stable jetting and absence of satellite droplets, the EAP ink formulations must meet several requirements on their rheological properties (i.e. viscosity, surface tension and density) that define the droplet dynamics. These requirements can be formulated in terms of the Reynolds number *Re*, Weber number *We* and *Z* number (inverse of the Ohnesorge number *Oh*) [43]:

$$Z = Oh^{-1} = \frac{Re}{\sqrt{We}} = \sqrt{\gamma \rho \alpha}/\eta, \qquad (1)$$

where ρ is the density of the fluid, η is its dynamic viscosity, γ is the surface tension, and α is the characteristic length (nozzle diameter). In a *We–Re* plot an inkjet-compatible ink needs to meet four constraints, illustrated as a box A–B–C–D in figure 5 [44, 45]: (1) the $We = 4$ line (A–B, yellow) represents the energy threshold for droplet ejection; (2) the $Z = 1$ line (A–D, orange) represents the higher viscosity bound, i.e. at $Z < 1$ the ink is too viscous for jetting; (3) the $Z = 14$ line (B–C, blue) represents the lower viscosity bound, i.e. at $Z > 14$ the ink forms satellite droplets; and (4) the $K_c = 100$ line (D–C, purple) indicates the onset of splashing upon impact with the substrate [46], requiring:

$$K_c = We^{1/2} \cdot Re^{1/4} \leqslant 100. \qquad (2)$$

While the *Z* numbers between 1 and 14 have been reported printable [45], this is not a general consensus between different studies [47, 48]. Figure 5 therefore also indicates a more conservative range of $4 \leqslant Z \leqslant 10$ that is agreed as printable jettable between several sources [45, 47, 48].

2.2.2. EAP ink formulation. EAP inks for printing the actuators are formulated from the P(VDF-TrFE-CTFE) polymer powder (Piezotech RT-TS, Arkema) [34]. It has a molecular weight of 400–600 kg mol^{-1} and CTFE content of 8.5 mol%. Ink formulation consists of choosing a suitable solvent composition and polymer concentrations, as explained in the following.

While a multitude of solvents could be used for dissolving the polymer [21, 34], this study used a mixture of MEK and DMSO. MEK (from Sigma-Aldrich) was chosen as the main solvent since it dissolves the piezopolymer very well [34]. Due to its high volatility (boiling point 79.6 °C), MEK evaporates fast from the printhead nozzles, leaving the polymer behind and causing the nozzles to clog. Therefore, MEK was combined with DMSO (Sigma-Aldrich), which also dissolves the polymer and has a higher boiling point (189 °C). Solvents with an even higher boiling point (>200 °C) were avoided, since they would significantly increase the solvent evaporation time
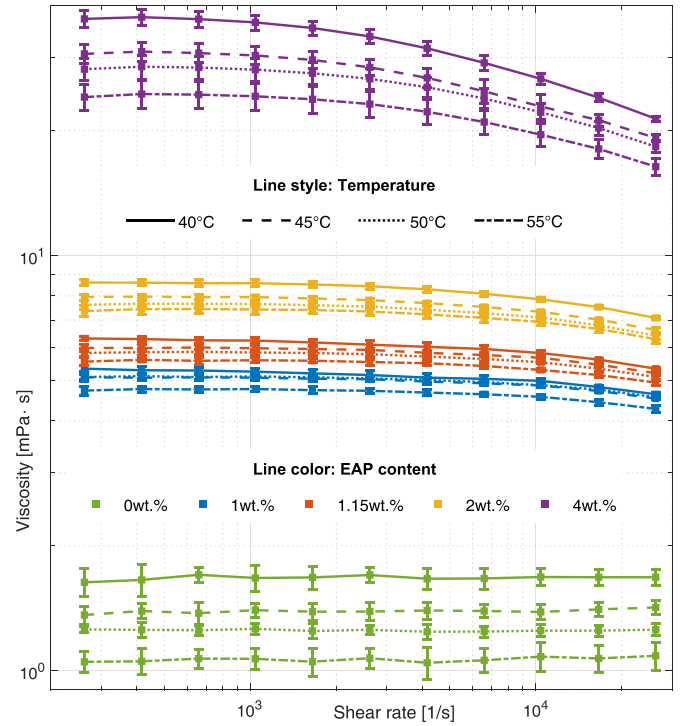

Figure 4. Dynamic viscosity measurement results for the 20:80 MEK:DMSO solvent ratio at EAP concentrations of 0 wt.%–4 wt.%.

after the printing. The selected solvents are chemically compatible with the components of the printheads.

The viscosities and surface tensions of different MEK:DMSO ratios (pre-mixing ratios of 60:40, 50:50, 40:60, 30:70 and 20:80 in volume) were experimentally measured using a rheometer (Anton Paar 302) and a contact angle meter (Data Physics OCA25) respectively. This indicated the 20:80 MEK:DMSO ratio (i.e. 15% wt.% MEK, $\gamma = 26.67$ mN m^{-1}, $\eta = 1.97$ cP, $\rho = 1.03$ g ml^{-1}) as the best-suited, exhibiting near-Newtonian behaviour, desirable in IJP. A similar solvent composition has been reported in formulating P(VDF-TrFE) inks in [21].

Next, the effect of the polymer concentration on the ink jettability was studied. The 20:80 MEK:DMSO solvent was loaded with different polymer concentrations between 0 wt.% and 4 wt.%. The polymer powder was incrementally added to the pre-mixed solvent, and the mixture was constantly stirred and heated up to 35 °C on a hot-plate (Cole–Parmer Stuart) over a period of 2 h. The viscosity and surface tension of the formulated piezopolymer inks were measured (Anton Paar 302, Data physics OCA25), as reported in figure 4 and table 2. The Reynolds and Weber numbers of the ink-printhead combinations were calculated to further evaluate their feasibility for stable jetting, considering the nozzle dimensions of both the Dimatix DMC (10 pl) and Konica Minolta KM512 (14 pl) printheads. The results for different ink formulations are respectively given in the figures 5 and 6. Addition of the polymer increases the surface tension and viscosity of the ink, and increases the droplet breakup time to inhibit the formation of satellite droplets. This allows to tailor the ink properties

Table 2. Surface tension measurement results for the EAP inks.

	Surface tension γ and its standard deviation std (mN m^{-1})									
EAP concentration	1 wt.%		1.15 wt.%		1.25 wt.%		2 wt.%		4 wt.%	
Temperature	γ	std	γ	std	γ	std	γ	std	γ	std
40 °C	35.431	0.218	35.904	0.210	35.934	0.234	36.187	0.197	37.185	0.203
45 °C	35.220	0.147	35.674	0.123	35.697	0.197	36.119	0.190	37.015	0.214
50 °C	35.106	0.210	35.519	0.109	35.545	0.183	36.023	0.206	36.824	0.234
55 °C	34.799	0.186	35.343	0.166	35.477	0.176	35.978	0.186	36.781	0.199
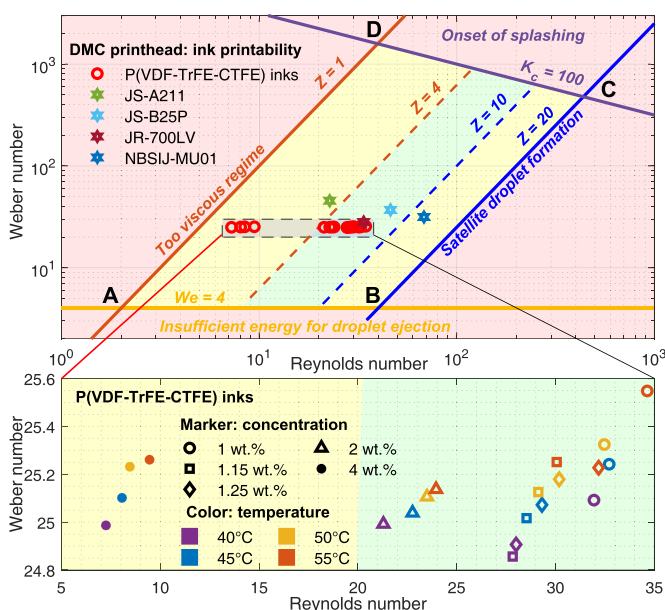
Figure 5. A rheological feasibility plot for printing the conductive and polymeric inks in the 10 pl DMC printhead (top). The zoom-in (bottom) details the properties of the EAP inks.
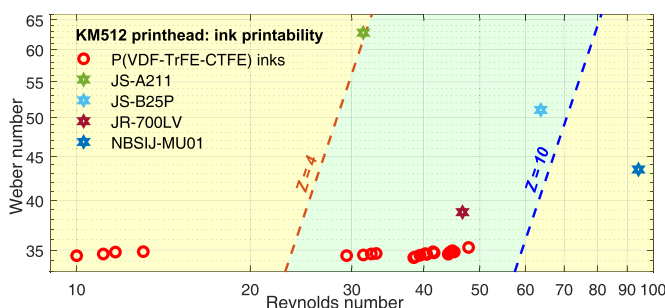
Figure 6. A rheological feasibility plot for printing the inks in the KM512 printhead. The relative placement between different inks is identical to the figure 5, while the absolute numbers are shifted due to a different nozzle diameter.

into a compatible range for IJP (see section 2.2.1). Viscosity measurements at different temperatures indicate that higher polymer concentrations can be printed at elevated temperatures (see figures 4–6).

2.3. EAP layer fabrication

This section describes the printing and curing processes of the EAP layer fabrication. EAP printing in section 2.3.1 covers the waveform formation for droplet jetting and substrate temperature settings to attain a uniform print. Section 2.3.2 explains the process of annealing and how it alters the EAP layer morphology.

2.3.1. Printing the EAP layer.
This study uses the Konica Minolta KM512 (14 pl nominal droplet volume) and Fujifilm Dimatix DMC (10 pl) printheads for polymer deposition. According to the rationale and process in section 2.2, two distinct inks with 1.25 wt.% and 1.15 wt.% polymer concentrations were formulated, respectively for the KM512 and DMC printheads. This was required due to different nozzle dimensions of the printheads. The inks were filtered through a 0.45 μm PTFE filter to prevent possible contaminant particles from clogging the nozzles, and then loaded into the printhead reservoirs.

To create reliable printing processes for the formulated inks it is necessary to establish jetting parameters that produce stable droplets with uniform velocity, volume and shape, with no satellite droplets. Establishing these parameters is facilitated by the DropView analysis tool (Pixdro LP50), allowing to inspect the droplets while adjusting the pulse shape, frequency, printhead temperature and ink pressure. Figure 3 shows the established pulse shapes for printing the EAP inks on both the KM512 and DMC printheads, and illustrates the resulting droplets with near-uniform characteristics. Jetting of all the nozzles is examined before each print cycle, and only the properly functioning nozzles are used for the printing. On average it was possible to use 49% of the KM512 nozzles and 75% of the DMC nozzles.

Printing settings for depositing the polymer layer are given for both the printheads in table 3. Droplet spacing and deposition rate are controlled via the printing resolution and repetition count. Solvent evaporation rate during the printing is controlled via the printbed temperature and introducing pauses between the printing cycles. It is desirable to evaporate most of the solvent before depositing a new layer of ink, in order to prevent ink from spreading, and to attain a more homogeneous polymer surface. In contrast, keeping the substrate table at the

Table 3. Printing settings and ink properties in the EAP layer deposition step.

Specification	KM512	DMC
Nominal droplet volume (pl)	14	10
Polymer concentration (wt.%)	1.25	1.15
Solvent composition (wt.%)	MEK 20:80 DMSO	MEK 20:80 DMSO
No. of printed layers	260	280
Substrate table temperature ($^{\circ}$C)	52.5	58
No. of active nozzles	ca 250 (out of 512)	ca 12 (out of 16)
Print speed (mm s^{-1})	110	90
Resolution (DPI)	750	800
Drop spacing (μm)	ca 34	ca 32
Pause cycle (repetitions)	80–80–60–40	80–80–80–40
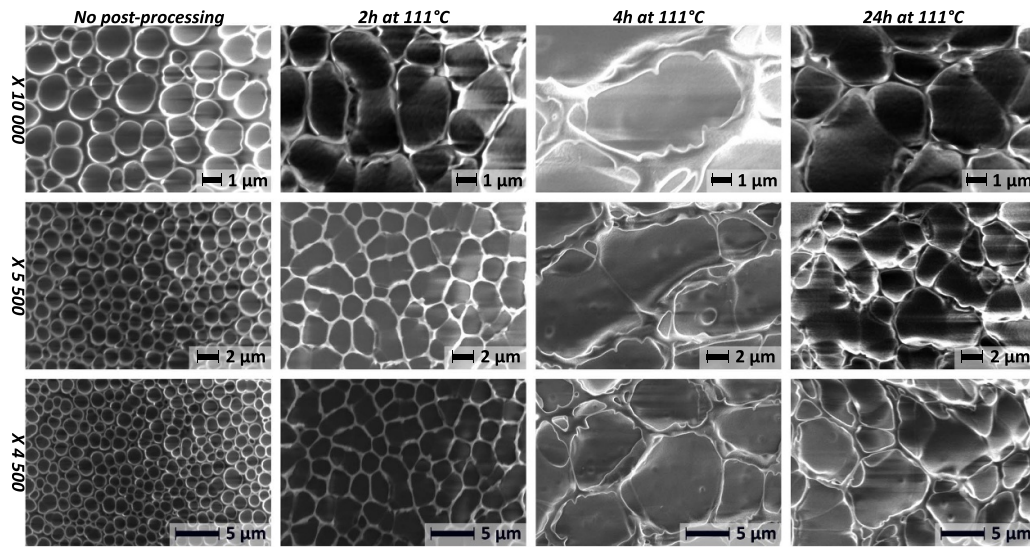
Figure 7. SEM images visualising the influence of the annealing time on the EAP morphology.

room temperature often resulted in a non-homogeneous polymer surface due to the coffee ring effects. In both the recipes the printbed was maintained at 65 $^{\circ}$C , and after a number of print repetitions (see table 3) a pause of 20 min (or longer) was held before resuming.

2.3.2. Annealing the EAP layer.
After printing, the polymer requires thermal annealing to improve its ferroelectric, piezoelectric and dielectric properties [49]. Annealing modifies the polymer microstructure and needs to be performed at 10 $^{\circ}$C–15 $^{\circ}$C below its melting temperature of 122 $^{\circ}$C [34, 50]. At lower temperatures the annealing is inefficient, and at higher temperatures it reduces the crystallinity, degrading the electromechanical response [50]. In actuator fabrication the annealing was performed for 2 h at 111 $^{\circ}$C .

The effect of annealing duration on the polymer surface morphology was studied by annealing the inkjet-printed P(VDF-TrFE-CTFE) samples at 111 $^{\circ}$C for up to 24 h. Morphology of the resulting EAP layer was imaged using a scanning electron microscope (SEM, Jeol JSM 6010LA). The results indicate that longer annealing durations increase the grain size and reduce the surface roughness (see figure 7). As

shown by Cho *et al* [51], exposure to elevated temperatures of the thermal annealing causes loss of β-phase, reduces ferroelectricity and deteriorates transduction performance in P(VDF-TrFE-CTFE). They proposed a solvent annealing method that can be used as an alternative to the thermal annealing, allowing to attain better transduction performance.

2.4. Top electrode fabrication

Fabrication of the top electrode comprises of functionalising of the polymer surface (section 2.4.1), inkjet printing of the Ag electrode (section 2.4.2), and sintering of the printed electrode to make it conductive (section 2.4.3).

2.4.1. Surface pre-treatment.
After thermally annealing the printed EAP layer (section 2.3.2) it is necessary to pre-treat its surface before the top electrode can be deposited on it. An untreated EAP surface is hydrophobic, disrupting the formation of a thin film during the printing, and causing the ink to agglomerate into droplets (see figure 8). Oxygen plasma treatment (Diener Femto plasma cleaner) is employed to functionalise the surface of the EAP layer and turn it hydrophilic. First,
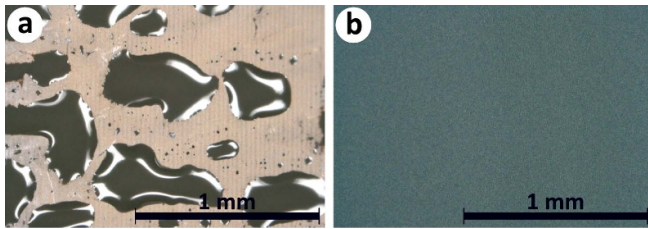
Figure 8. Printing the top electrode on the annealed EAP layer: (a) without plasma treatment the ink agglomerates into droplets; (b) uniform electrode can be printed after oxygen plasma treatment.

the effect of the plasma exposure time was experimentally studied by exposing EAP samples for different durations (10–150 s) and then printing Ag electrodes on them. The results showed the best wettability and layer quality after 30 s of exposure, which was long enough to clean and form hydroxyl groups on the surface and short enough to avoid thermal damage. The difference in the electrode deposition quality between the treated and untreated samples is shown in figure 8. Hydrophobic recovery caused a drastic deterioration in the wettability and deposition quality after 2 h post-treatment, possibly due to the loss of hydroxyl groups and reconfiguration of the surface layer. Hydrophobic recovery is a known phenomenon in polymers [52], while the specific reasons for it in the PVDF-based materials need investigation.

2.4.2. IJP the top electrode. The top electrode is printed on the plasma-treated EAP layer using a Dimatix DMC 10 pl printhead, loaded with the NovaCentrix JS-A211 ink (40 wt.% Ag content) [37]. A different ink than in the bottom electrode manufacturing (section 2.1) is used, since the self-sintering inks with a low Ag loading factor require a porous substrate (15 wt.% Ag in Mitsubishi NBSIJMU01). On a smooth EAP layer they cannot self-sinter, and develop cracks or partial delaminations during the sintering (see figure 9). Similar observations were also made for the NovaCentrix JS-B25P self-sintering ink (25 wt.% Ag). Behaviour of the inks on a plasma-treated EAP surface is contrasted in figure 9.

The printing settings for depositing the top electrode on the EAP layer are given in table 1, and the established waveform for jetting the JS-A211 ink is given in figure 3(a). The printing is carried out at a substrate table temperature of 65 °C to prevent the coffee ring effects from occurring (similar to section 2.3.1). After solvent evaporation this produced a crack-free, homogeneous surface that is not conductive until post-processed.

2.4.3. Sintering the top electrode. To attain a conductive top electrode, the printed Ag particles must be fused together into a conductive layer. Sintering the Ag ink was studied by thermal means (Memmert UN30 convection oven), strobe lamp (150 W), pulsed UV laser (Optec WS-Starter with a SpectraPhysics Talon 355-15 source) and continuous UV light source (Phoseon FireEdge FE300, in Pixdro LP50). The latter relies on matching the wavelength of a UV source with the

plasmonic resonance absorption peak of the Ag particles, allowing efficient sintering at low intensities [53]. For the 30–50 nm particles of the JS-A211 ink [37] this peak lies between ~400–420 nm [53], sufficiently close to the wavelength of the continuous UV source in the Pixdro LP50 printer (345–385 nm).

Conductivity of the sintered samples was confirmed by measuring the resistance along the electrode length using a multimeter (Voltcraft VC820-1). All sintering methods turned the electrode conductive, resulting in the electrode resistances of $\geqslant 0.5\,\Omega$ for the strobe light, $\geqslant 3.8\,\Omega$ for the thermal method (causes also samples to significantly curl), $\geqslant 16\,\Omega$ for the laser source, and $\geqslant 2.7\,\Omega$ for the continuous UV source. These figures are better than needed for actuation [27]. The resulting electrode morphologies are compared in figure 10, showing a continuous porous (most likely due to densification and solvent evaporation) silver surface in all samples. While the strobe light attained the best conductivity, sintering with the continuous UV source was faster and less laborious than other methods (built-in tool in the LP50 printer), producing undamaged, shiny, crack-free electrode surface without excessively heating the sample. The best results were obtained after a 360 s exposure at $0.6\,\mathrm{W\,cm^{-2}}$ intensity. The sintering was assisted by heating the substrate table to 40 °C, speeding up the evaporation of the remaining solvent from the ink.

Therefore, the continuous UV source of the Pixdro LP50 system and the above recipe are used to cure the top electrode during the subsequent actuator fabrication. After the curing, the actuator sample is cut out from the rectangular substrate using an Optec WS Starter laser micromachining system.

2.5. Characterising actuator morphology

To characterise the outcomes of the fabrication process, morphology of the resulting actuator was studied in SEM. Both the KM512 and DMC actuator samples were cut in a laser micromachining system (Lasea LS Lab) to reveal their cross-section, and imaged in SEM (JEOL JSM 6010LA). Thicknesses of all the printed layers (i.e. bottom electrode, active layer and top electrode), substrates and the total actuator thicknesses were measured. These results allow to link the deposition recipes to the resulting layer thicknesses for further optimisation of the manufacturing process.

2.6. Characterising actuator performance

Performance of the fabricated actuators was characterised by measuring their response to sinusoidal excitation, the effect of input voltage amplitude on the actuation amplitude, the actuation hysteresis, and the frequency response. An experimental set-up was constructed for this purpose, as explained in figure 11.

A completed actuator sample was attached by its base to a custom-built clamp (3D-printed, PET-G), fixing the actuator in a horizontal configuration. Actuator terminal pads
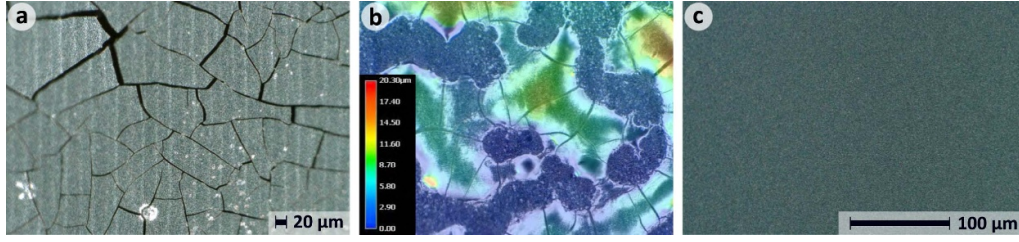
Figure 9. Printing different types of Ag inks on the EAP surface. Inks that are intended for porous substrates form cracks (a) and droplets (b) when printed on the EAP. Inks intended for smooth substrates yield a uniform conductive layer (c).
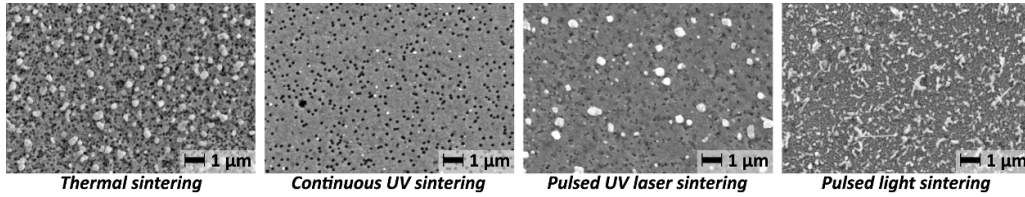

Figure 10. SEM images visualising the influence of different sintering approaches on the morphology of the top electrode. The residues on the sample surfaces are hypothesised to be the fluoropolymer binder residues from the JS-A211 ink [37].
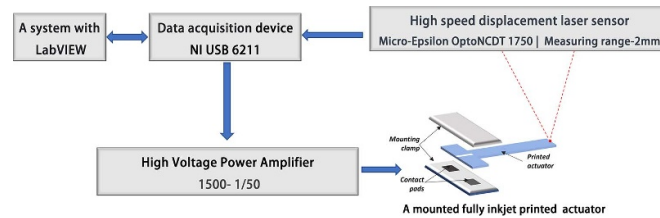

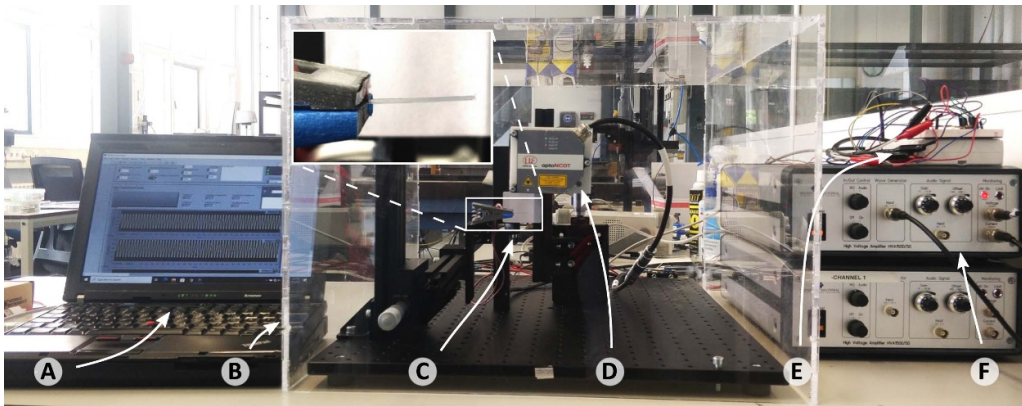**Figure 11.** Block diagram of the actuator performance characterisation set-up.

Figure 12. The experimental set-up for actuation performance characterisation: *A*—PC with the NI LabView environment; *B*—transparent acrylic box; *C*—clamped actuator; *D*—laser displacement sensor; *E*—data acquisition system; and *F*—high-voltage power amplifier.

made contact with the silver electrodes of the clamp, providing the electrical connections for excitation. Conductive silver paste (RS Pro 186-3600) was used on the actuator terminals to improve the conductivity and wear resistance at the contacts. The actuator was driven by a high voltage power amplifier (Smart Material HVA 1500-1/50), and its tip displacements were measured using a laser triangulation sensor (Micro-Epsilon OptoNCDT 1750, range of 2 mm). Thorlabs mounting components and translation stages were used to fix and align the actuator and the laser. The experiments were controlled from a PC with the LabView 2018 environment, using a NI USB-6211 data acquisition board. A block diagram and an image of the set-up are shown in figures 11 and 12 respectively. The setup was enclosed in a transparent acrylic box with a safety switch, that is connected to the interlock of the high-voltage amplifier.

For characterisation, experiments were conducted to measure the actuator's (1) response to quasi-static excitation (1 Hz sine wave), (2) deflection amplitude dependency on the input voltage magnitude, (3) hysteresis during cyclic actuation, and

(4) frequency response. Experiments (1)–(3) were conducted using a sinusoidal excitation at 1 Hz frequency, maintaining the effects of the beam dynamics negligible. Experiment (4) performed a frequency sweep in order to measure the dynamic response. Uni-polar sinusoidal excitation is used in experiment (1) since the ferroelectric behaviour of the actuators is independent of the polarity, and in experiment (4) since a bipolar input would result in the actuation output to occur at double of the input frequency. Frequency response measurements were conducted at 75 V amplitude, 75 V offset (i.e. 150 V_{pp}), applied at 100 different frequencies that are logarithmically distributed in the 1–200 Hz interval. Bipolar sinusoidal excitation was used in the experiments (2) and (3), allowing to observe the presence of permanent piezoelectric effect in the polymer, which would express in a polarity- and voltage-dependent asymmetry in the actuation amplitude.

3. Results

Actuator samples were successfully manufactured according to the design in figure 1, following the methodology and the two recipes described in sections 2.1 through 2.4. Since the recipes only differ in active layer printing step (section 2.3), the resulting samples (shown in figure 13) are addressed according to the respective printhead models as *KM512* and *DMC*. The resistances between the actuator electrodes measured in the order of MΩ, indicating an undamaged EAP layer.

3.1. Morphology

Actuator morphology was studied according to the section 2.5. SEM images of the actuator cross-sections for both the *KM512* and *DMC* samples are shown in figure 14. Thickness measurement results from these images are summarised in table 4 for each layer. The total thicknesses of the actuators measured 125 μm (*KM512*) and 131 μm (*DMC*). The bottom electrodes were poorly visible, measuring $<1\,\mu$m in both samples, while the top electrodes were respectively 3.64 μm (*KM512*) and 1.72 μm (*DMC*) thick. The EAP layer in the *KM512* sample measured 6.38 μm, meaning a 24.5 nm deposition thickness per each print repetition (total 260 prints). In the *DMC* sample the EAP layer was 6.35 μm thick, i.e. 22.7 nm per print repetition (total 280 prints).

3.2. Actuation

The performance characterisation experiments were performed according to the section 2.6. Actuator placement and oscillating tip deflections are shown in figure 15 and **video 1**. In the preliminary experiments it was observed that actuator damage occurs at voltages above 200 V and 275 V respectively in the *DMC* and *KM512* samples. These voltages correspond to the maximum electric field strengths of 31.5 V μm^{-1} (DMC) and 43.1 V μm^{-1} (KM512), and were not exceeded the characterisation experiments.

Actuation in response to a 1 Hz sinusoidal excitation is plotted in figure 16, showing maximum deflections of 91.4 μm (200 V) and 224 μm (275 V) respectively for the *DMC* and
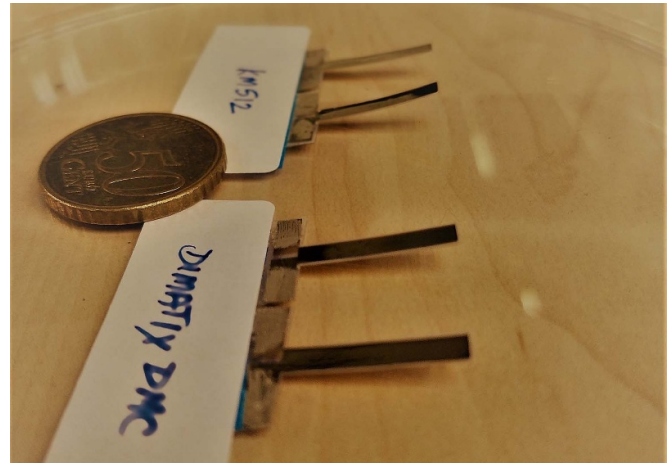

Figure 13. The manufactured actuator samples.

KM512 samples. The effect of the excitation voltage amplitude on the actuation response is shown in figure 17. Presuming a quadratic voltage–displacement relationship, the actuation gains of $\alpha_1 = 2.28$ nm V^{-2} and $\alpha_2 = 3.27$ nm V^{-2} were fitted to the measured displacement data.

Actuation hysteresis curves in response to a bipolar sinusoidal excitation (1 Hz, 200 V) are given in figure 18. No polarity- or voltage-dependent asymmetry was observed in the actuation amplitude, indicating no presence of permanent piezoelectric effect. Results for the frequency response measurement are plotted in figure 19 (unipolar excitation, 150 V_{pp}), indicating that the resonant frequencies for the *DMC* and *KM512* actuator samples are respectively 113 Hz and 114 Hz. When excited with a unipolar 200 V_{pp} excitation at their resonant frequencies, these actuators respectively achieved 1.10 mm (*DMC*) and 1.72 mm (*KM512*) deflections. The effective elastic moduli and the blocked actuation forces were respectively estimated to be 1.23 GPa and 0.15 mN for the *DMC* sample, and 1.57 GPa and 0.41 mN for the *KM512* sample.

4. Discussion

4.1. Manufacturing

After establishing stable jetting parameters, printing of the bottom electrode produced consistent results throughout this work. While the chosen ink-substrate combination (i.e. Mitsubishi NBSIJ-MU01 and Novele IJ-220) allowed to reduce the number of fabrication steps, the same method does not work on smooth polymer surfaces, such as polyimide or PEN. A similar method to the top electrode fabrication can be used in this case, i.e. functionalising the surface with oxygen plasma, printing the bottom electrode using the JS-A211 ink, and UV-curing it.

The EAP inks were formulated as described in section 2.2, and then printed and annealed as described in section 2.3. Initially a KM512 printhead was used for the EAP layer deposition; however its heating circuit failed mid-study, possibly due to a damage by the aggressive solvents. Therefore, a Dimatix
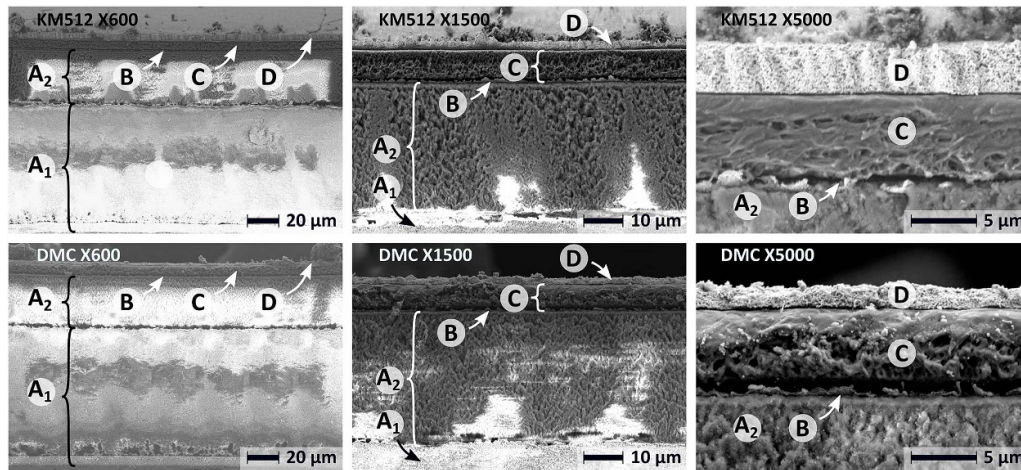
Figure 14. SEM images of the actuator cross-sections (JEOL JSM 6010LA): a *KM512* sample in the top row, and a *DMC* sample in the bottom row. *A*—Novele IJ-220 PEN substrate (A_1) with the microporous resin coating (A_2); *B*—bottom electrode; *C*—P(VDF-TrFE-CTFE) layer; and *D*—top electrode.

Table 4. Dimensions of the actuator layers (measured in SEM).

Layers\samples	KM512	DMC
Top electrode	$3.64\,\mu\text{m}$	$1.72\,\mu\text{m}$
Active layer	$6.38\,\mu\text{m}$	$6.35\,\mu\text{m}$
Bottom electrode	$<1\,\mu\text{m}$	$<1\,\mu\text{m}$
Substrate	$114\,\mu\text{m}$	$123\,\mu\text{m}$
Entire actuator	$125\,\mu\text{m}$	$131\,\mu\text{m}$

DMC printhead was used also for EAP deposition in the remainder of the work, requiring a dedicated EAP ink formulation. Ink composition is a trade-off between reliable jetting and deposition rate. While the higher concentrations allow depositing more polymer per droplet, their jetting is less repeatable and clogging occurs more frequently (see section 2.2.1). Optimal waveform and printing settings depend on the ink properties and printhead characteristics, and were obtained via trial-and-error.

The challenges in top electrode fabrication were resolved by first applying oxygen plasma treatment on the EAP layer to make it hydrophilic, then printing the electrode using a dedicated Ag ink for smooth substrates, and eventually curing it via heating and UV exposure. Differences in the top electrode thicknesses are hypothesised to stem from the variation in the DMC cartridge performance over time (affects the droplet volumes), and from the flowing of the wet ink on the EAP layer (stimulated by the printbed motion) that causes its non-uniform re-distribution. Plasma treatment and annealing of the EAP layer (section 2.3.2) were performed outside the printer, and in future work it is desirable to substitute these steps with alternatives that allow the entire fabrication process to be completed within the printer.

4.2. Characterisation

The *KM512* sample deflected upon 1 Hz excitation 2.45 times more than the *DMC* sample, and withstood higher voltages before break-down (see figures 16 and 17). At the lowest sinusoidal excitation voltage amplitude (50 V) the *DMC* sample performed better than the *KM512*, while withstanding significantly lower maximum voltages (200 V for *DMC* and 275 V for *KM512*). We therefore hypothesise that the EAP layer in the *DMC* samples is much less uniform compared to the *KM512*, resulting in larger variations in the local electric field strengths. This would certainly affect actuation due to the quadratic relation between the strain and electric field strength. Variations in the EAP layer uniformity can stem from the printing process or sensitivity towards other steps in the manufacturing process. While the deposited EAP layer thickness differs between the samples by $<0.5\%$ in the measurements (table 4) and by $<6\%$ in the calculations (see droplet volumes, DPIs, concentrations and layer counts in table 3), the higher local variations in the *DMC* sample can stem from the less repeatable deposition quality of the DMC printhead (e.g. jetting stability in the start and middle of a print line, and variation in the droplet volumes).

In both actuator types the maximum field strengths ($31.5\,\text{V}\,\mu\text{m}^{-1}$ for *DMC* and $43.1\,\text{V}\,\mu\text{m}^{-1}$ for *KM512*) remained significantly below the dielectric strength of the P(VDF-TrFE-CTFE), i.e. $\geqslant 350\,\text{V}\,\mu\text{m}^{-1}$ [33, 34]. We hypothesise that this is caused by the same local imperfections in the EAP layer thickness. Other possible causes include contaminants that may fallen from the air during the printing process, and non-perfect densification of the EAP layer during the solvent evaporation and annealing steps.

The achieved actuation deflections (i.e. 1.72 mm at 114 Hz, $224\,\mu\text{m}$ quasi-static) are a significant improvement over the priorly reported results for the entirely inkjet-printed bending cantilever actuators. In comparison, Pabst *et al* (actuator length 15 mm) attained $145\,\mu\text{m}$ and $300\,\mu\text{m}$ deflections respectively in static and resonant (160 Hz) operation [29], while Thuau *et al* reported 1.5 nm deflections for their 5 mm long actuators [7]. This means at least a 55% improvement in quasi-static and 470% in resonant deflections. Compared to best partially IJP'ed actuators, this is above the $206\,\mu\text{m}$ quasi-static
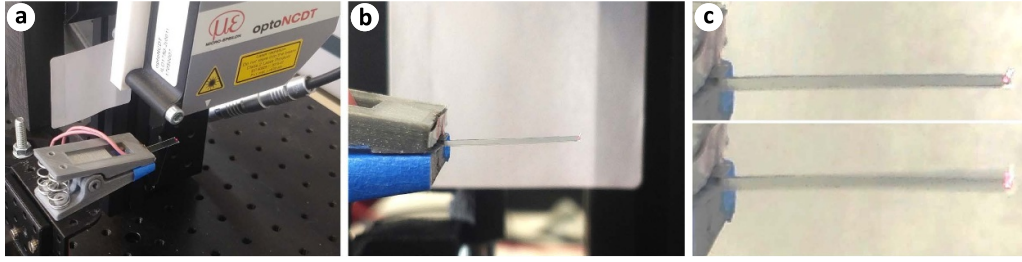
Figure 15. Actuation experiments: (a) actuator placement in the experimental set-up; (b) side view of the clamped actuator; and (c) screenshots of the actuator when still (top) and oscillating (bottom) (**video 1**).
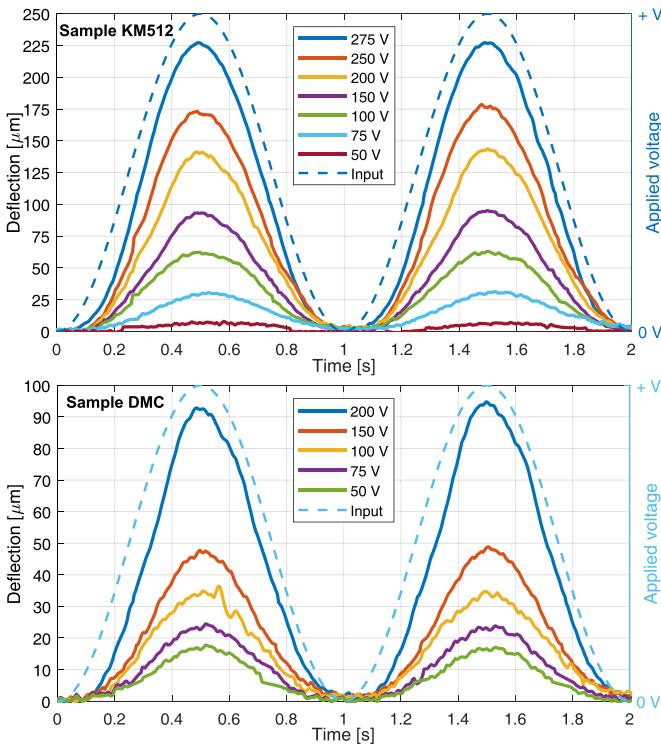

Figure 16. Actuation in response to a sinusoidal excitation at 1 Hz. Top—*KM512* sample; and bottom—*DMC* sample.

Figure 17. Actuation in response to a 1 Hz sinusoidal excitation at different excitation voltage amplitudes. Experimental results and curve-fitted quadratic models ($\alpha_1 = 2.28\,\mathrm{nm\,V^{-2}}$, $\alpha_2 = 3.27\,\mathrm{nm\,V^{-2}}$).
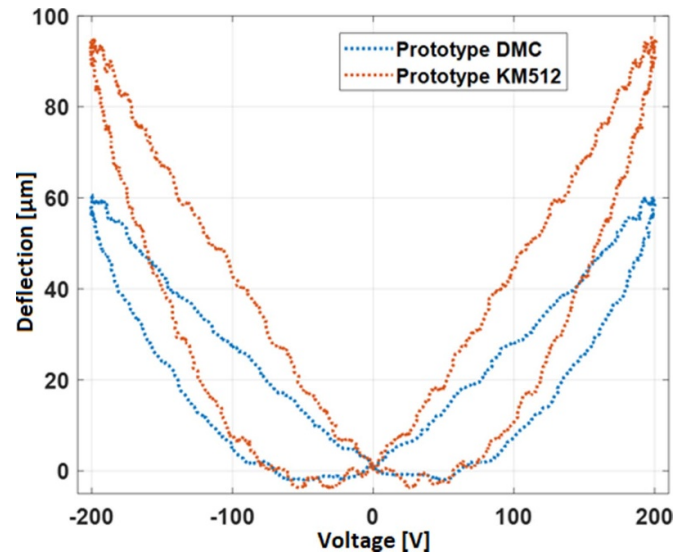
Figure 18. Actuation hysteresis under a 1 Hz 200 V bipolar sinusoidal excitation.

deflections reported by Baelz and Hunt [26], but less than their resonant deflections of 3 mm.

High actuation strains in this study stem from the high-strain P(VDF-TrFE-CTFE) relaxor ferroelectric material. Poling of the P(VDF-TrFE-CTFE) has been shown to further increase the actuation strains by about 18% [26]. Stiffness, force and stroke characteristics of a bending cantilever actuator are a trade-off between the active and constraining layer thicknesses and elastic moduli [54, 55]. Therefore, a significant performance improvement can be attained by optimising the actuator mechanical compliance via the EAP and substrate thicknesses (now EAP makes <6% of the total thickness) and choice of materials. For example, choosing a substrate that is very thin and soft to the bending while being very stiff in the axial direction can reduce the axial extension of the actuator (useless for actuation) and increase the lateral
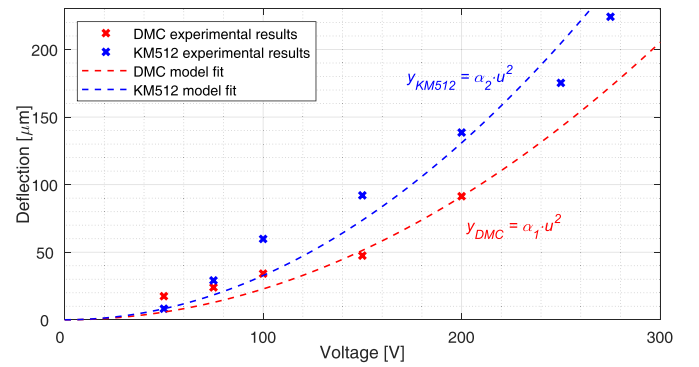
deflections. Actuation voltages can be lowered by printing a stack of thinner EAP layers, alternated with electrode layers. The future work will address the above challenges, and aim to reduce the fabrication complexity to increase the process throughput.
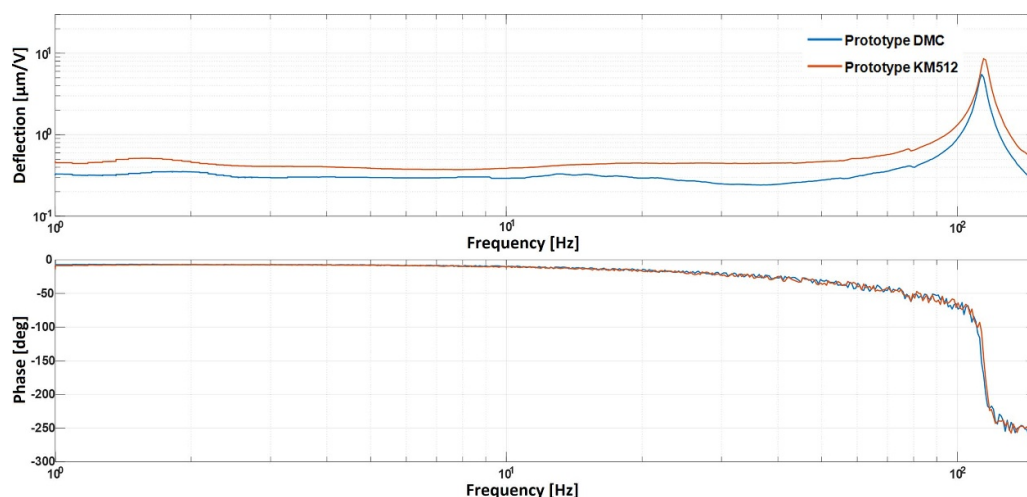
Figure 19. Bode plots of the inkjet-printed actuators, measured under a sinusoidal excitation with a 75 V amplitude and 75 V offset (i.e. 150 V_{pp}). Applying an offset prevents the frequency doubling due to the ferroelectric actuation response.

4.3. Outlook

Compared to the traditional methods of fabricating smart material transducers (screen-printing, doctorblading, spin-coating, painting, sputter-coating, etc), IJP provides the virtues of a digital and contact-less means of fabrication: (1) it eliminates the need for design-specific masks, enabling implementation of complex designs, patterns and voids, virtually limited only by the in-plane resolution of the printer; and (2) it allows fine (sub-micron) thickness resolutions, essential for attaining high field strengths within the EAP layers at low operational voltages. While the total fabrication time remains limited by the processing steps (i.e. deposition, solvent evaporation, curing and annealing), further automation of these processing steps is feasible. The latter provides outlooks for further minimisation of the involved human labour. A well-established IJP process enables automated implementation and modification of bespoke transducer designs, without sacrificing the actuation performance. Similar actuators with IJP'ed electrodes and spin-coated EAP layer (based on the identical substrate and EAP materials) were seen to perform similarly (i.e. inferior in quasi-static and better in resonant operation) [26]. Looking further into future, resolving challenges in integration of the IJP of increasingly dissimilar and delicate materials is anticipated to enable integrated printing of mechanisms, electronics and transducers, leading towards printing of entire mechatronic systems and devices of bespoke design in a single and efficient process.

5. Conclusion

This research developed a process for additive manufacturing P(VDF-TrFE-CTFE)-based EAP actuators. The process bases on IJP and consists of three main steps: (1) depositing the bottom electrode by printing a self-sintering Ag ink on a PET-based substrate; (2) fabricating the EAP layer on the bottom electrode by printing a custom-formulated P(VDF-TrFE-CTFE) ink, and thermally annealing it; and (3) depositing the top electrode by printing an Ag ink on the plasma-activated

EAP surface and then UV-curing it. Depositing the bottom electrode was relatively straight-forward. The challenges were encountered in the formulation, printing and curing of the P(VDF-TrFE-CTFE) ink in the EAP layer fabrication step, and in the deposition, adhesion and sintering of the Ag ink in the top electrode fabrication step. Functional actuator samples were manufactured using two different printheads for the EAP layer deposition.

The resulting *DMC* and *KM512* samples respectively produced 91.4 μm (200 V_{pp}) and 224 μm (275 V_{pp}) deflections upon 1 Hz sinusiodal excitation. In resonant operation the same actuators respectively produced 1.10 mm (113 Hz, 200 V_{pp}, *DMC*) and 1.72 mm (at 114 Hz, 200 V_{pp}, *KM512*) deflections. This is a 55% improvement in quasi-static displacements and a 470% improvement in resonant displacements over the previously reported fully inkjet-printed PVDF-based actuators, and an 8% improvement in quasi-static displacements over the similar partially inkjet-printed actuators. The observed actuation hysteresis and voltage–displacement relationships were consistent with the ferroelectric behaviour.

This is the first time that a relaxor ferroelectric actuator has been entirely fabricated via IJP. The resulting actuators showed a significant improvement in actuation displacements, essential for complementing the printed electronics to enable printed mechatronics. The future work will further address the challenges in actuation performance and reducing the fabrication complexity.

Data availability statement

All data that support the findings of this study are included within the article (and any supplementary files).

ORCID iDs

S A Sekar ⬡ https://orcid.org/0009-0009-2892-871X
A Hunt ⬡ https://orcid.org/0000-0001-5350-7719

References

[1] Cui Z 2016 *Printed Electronics* (Wiley) ch 1, pp 1–20

[2] Espera A H, Dizon J R C, Chen Q and Advincula R C 2019 3D-printing and advanced manufacturing for electronics *Prog. Addit. Manuf.* **4** 245–67

[3] Tan H W, Choong Y Y C, Kuo C N, Low H Y and Chua C K 2022 3D printed electronics: processes, materials and future trends *Prog. Mater. Sci.* **127** 100945

[4] Ikram H, Rashid A A and Koç M 2022 Additive manufacturing of smart polymeric composites: literature review and future perspectives *Polym. Compos.* **43** 6355–80

[5] Engel K E, Kilmartin P A and Diegel O 2022 Recent advances in the 3D printing of ionic electroactive polymers and core ionomeric materials *Polym. Chem.* **13** 456–73

[6] Lalegani Dezaki M and Bodaghi M 2023 A review of recent manufacturing technologies for sustainable soft actuators *Int. J. Precis. Eng. Manuf. Green Technol.* **10** 1661–710

[7] Thuau D, Kallitsis K, Dos Santos F D and Hadziioannou G 2017 All inkjet-printed piezoelectric electronic devices: energy generators, sensors and actuators *J. Mater. Chem.* **5** 9963–6

[8] Patpatiya P, Chaudhary K, Shastri A and Sharma S 2022 A review on polyjet 3D printing of polymers and multi-material structures *Proc. Inst. Mech. Eng.* C **236** 7899–926

[9] Stratasys 2021 3D printing applications in manufacturing: stratasys direct (available at: www.stratasys.com/en/stratasysdirect/applications/) (Accessed 26 October 2023)

[10] Liu Y, Cui T and Varahramyan K 2003 All-polymer capacitor fabricated with inkjet printing technique *Solid-State Electron.* **47** 1543–8

[11] Lemarchand J, Bridonneau N, Battaglini N, Carn F, Mattana G, Piro B, Zrig S and Noël V 2022 Challenges, prospects and emerging applications of inkjet-printed electronics: a chemist's point of view *Angew. Chem., Int. Ed.* **61** e202200166

[12] Nayak L, Mohanty S, Kumar Nayak S K and Ramadoss A 2019 A review on inkjet printing of nanoparticle inks for flexible electronics *J. Mater. Chem.* C **7** 8771–95

[13] Andò B and Marletta V 2016 An all-inkjet printed bending actuator with embedded sensing feature and an electromagnetic driving mechanism *Actuators* **5** 21

[14] Ta T D, Umedachi T and Kawahara Y 2019 Inkjet printable actuators and sensors for soft-bodied crawling robots *2019 Int. Conf. on Robotics and Automation (ICRA)* pp 3658–64

[15] Derby B 2010 Inkjet printing of functional and structural materials: fluid property requirements, feature stability and resolution *Annu. Rev. Mater. Res.* **40** 395–414

[16] Simaite A, Mesnilgrente F, Tondu B, Souéres P and Bergaud C 2016 Towards inkjet printable conducting polymer artificial muscles *Sens. Actuators* B **229** 425–33

[17] Galliani M, Ferrari L M, Bouet G, Eglin D and Ismailova E 2023 Tailoring inkjet-printed PEDOT:PSS composition toward green, wearable device fabrication *APL Bioeng.* **7** 016101

[18] Põldsalu I, Rohtlaid K, Nguyen T M G, Plesse C, Vidal F, Safaei Khorram M, Peikolainen A-L, Tamm T and Kiefer R 2018 Thin ink-jet printed trilayer actuators composed of PEDOT:PSS on interpenetrating polymer networks *Sens. Actuators* B **258** 1072–9

[19] Schmidt V H, Lediaev L, Polasik J and Hallenberg J 2006 Piezoelectric actuators employing PVDF coated with flexible PEDOT-PSS polymer electrodes *IEEE Trans. Dielectr. Electr. Insul.* **13** 1140–8

[20] Closson A, Richards H, Xu Z, Jin C, Dong L and Zhang J X J 2021 Method for inkjet-printing PEDOT:PSS polymer electrode arrays on piezoelectric PVDF-TrFE fibers *IEEE Sens. J.* **21** 26277–85

[21] Haque R, Vié R, Germainy M, Valbin L, Benaben P and Boddaert X 2015 Inkjet printing of high molecular weight PVDF-TrFE for flexible electronics *Flex. Print. Electron.* **1** 015001

[22] Liu Q, Le M Q, Richard C, Liang R, Cottinet P-J and Capsal J-F 2019 Enhanced pseudo-piezoelectric dynamic force sensors based on inkjet-printed electrostrictive terpolymer *Org. Electron.* **67** 259–71

[23] Banquart A, Callé S, Levassort F, Fritsch L, Ossant F'eric, Toffessi Siewe S, Chevalliot S, Capri A and Grégoire J-M 2021 Piezoelectric P(VDF-TrFE) film inkjet printed on silicon for high-frequency ultrasound applications *J. Appl. Phys.* **129** 195107

[24] Abdolmaleki H, Bjørnetun Haugen A, Merhi Y, Vinge Nygaard J and Agarwala S 2023 Inkjet-printed flexible piezoelectric sensor for self-powered biomedical monitoring *Mater. Today Electron.* **5** 100056

[25] Alique M, Moya A, Kreuzer M, Lacharmoise P, Murillo G and Delgado Simao C 2022 Controlled poling of a fully printed piezoelectric PVDF-TrFE device as a multifunctional platform with inkjet-printed silver electrodes *J. Mater. Chem.* C **10** 11555–64

[26] Baelz K and Hunt A 2019 P(VDF-TrFE-CTFE) actuators with inkjet printed electrodes *7th Int. Conf. on Control, Mechatronics and Automation (ICCMA)* pp 327–32

[27] Baelz K and Hunt A 2023 Printing electrodes for P(VDF-TrFE-CTFE) actuators using a consumer-grade inkjet printer *Proc. SPIE* **12482** 124820

[28] Pabst O, Perelaer J, Beckert E, Schubert U S, Eberhardt R and Tünnermann A 2011 Inkjet printing of electroactive polymer actuators on polymer substrates *Proc. SPIE* **7976** 717–22

[29] Pabst O, Perelaer J, Beckert E, Schubert U S, Eberhardt R and Tünnermann A 2013 All inkjet-printed piezoelectric polymer actuators: characterization and applications for micropumps in lab-on-a-chip systems *Org. Electron.* **14** 3423–9

[30] Ramadan K S, Sameoto D and Evoy S 2014 A review of piezoelectric polymers as functional materials for electromechanical transducers *Smart Mater. Struct.* **23** 033001

[31] Cheng Z-Y, Bharti V, Xu T-B, Xu H, Mai T and Zhang Q M 2001 Electrostrictive poly(vinylidene fluoride-trifluoroethylene) copolymers *Sens. Actuators* A **90** 138–47

[32] Solvay 2017 Solvene EAP for Printed Organic Electronics Techinal data sheet solvene 200 EAP pp 1–2 (available at: www.solvay.com/sites/g/files/srpend221/files/2018-10/Solvene-EAP-for-Printed-Electronics_EN-v2.3_0_0.pdf) (accessed 19 January 2024)

[33] Bauer F 2010 Relaxor fluorinated polymers: novel applications and recent developments *IEEE Trans. Dielectr. Electr. Insul.* **17** 1106–12

[34] Arkema P 2020 Techincal guide piezotech RT-TS pp 1–7 (available at: https://page.arkema.com/rs/253-HSZ-754/images/Technical%20Guide%20Piezotech%20RT-TS.pdf) (accessed 19 January 2024)

[35] NovaCentrix 2011 Novele™ IJ-220 printed electronics substrate - inkjet receptive p 1 (NCC Nano LLC) (available at: www.novacentrix.com/datasheet/Novele%20IJ-220.pdf) (accessed 19 January 2024)

[36] ChemTel Inc 2019 NBSIJ-MU01 (silver nano particle ink) safety data sheet pp 1–10 (available at: http://mitsubishiimaging.com/support/SDS/NBSIJ-MU01.pdf) (accessed 19 January 2024)

[37] Novacentrix 2020 Metalon® JS-A211 nanosilver ink - aqueous dispersion for inkjet printing (NCC Nano LLC)

(available at: www.novacentrix.com/datasheet/Metalon-JS-A211-TDS.pdf) (accessed 19 January 2024)

[38] SUSS MicroTec Specifications- pixdro lp50 (available at: www.suss.com/en/products-solutions/inkjet-printing/lp50) (accessed 19 January 2024)

[39] Kato Y 2014 FUJIFILM group's inkjet printhead and technology pp 27–31 (available at: www.ekkotech.com/file/Fuji%20Group%20Printhead%20&%20Technology.pdf) (accessed 19 January 2024)

[40] Konica Minolta Inc Specifications - Konica Minolta KM512 series (available at: https://www.konicaminolta.com/global-en/inkjethead/products/inkjethead/512/spec.html) (accessed 19 January 2024)

[41] Bevione M and Chiolerio A 2020 Benchmarking of inkjet printing methods for combined throughput and performance *Adv. Eng. Mater.* **22** 2000679

[42] Shen X, Ho C-M and Wong T-S 2010 Minimal size of coffee ring structure *J. Phys. Chem.* B **114** 5269–74

[43] Hutchings I M and Martin G D 2013 *Inkjet Technology: For Digital Fabrication* (Wiley) (https://doi.org/10.1002/9781118452943)

[44] Reis N, Ainsley C and Derby B 2005 Ink-jet delivery of particle suspensions by piezoelectric droplet ejectors *J. Appl. Phys.* **97** 094903

[45] Jang D, Kim D and Moon J 2009 Influence of fluid physical properties on ink-jet printability *Langmuir* **25** 2629–35

[46] Bathurst S 2012 Ink jet printing of PZT thin films for MEMS *PhD Thesis* Massachusetts Institute of Technology (available at: https://dspace.mit.edu/handle/1721.1/78236)

[47] Reis N and Derby B 2000 Ink jet deposition of ceramic suspensions: modeling and experiments of droplet formation *MRS Online Proc. Libr. (OPL)* **625** 117

[48] Liu Y and Derby B 2019 Experimental study of the parameters for stable drop-on-demand inkjet performance *Phys. Fluids* **31** 032004

[49] Wang J, Li Z, Yan Y, Wang X, Xie Y and Zhang Z 2016 Improving ferro- and piezo- electric properties of hydrogenized poly(vinylidene fluoride-trifluoroethylene) films by annealing at elevated temperatures *Chin. J. Polym. Sci.* **34** 649–58

[50] Ducrot P-H, Dufour I and Ayela C 2016 Optimization of PVDF-TrFE processing conditions for the fabrication of organic mems resonators *Sci. Rep.* **6** 01

[51] Cho Y *et al* 2016 Enhanced ferroelectric property of P(VDF-TrFE-CTFE) film using room-temperature crystallization for high-performance ferroelectric device applications *Adv. Electron. Mater.* **2** 1600225

[52] Jokinen V, Suvanto P and Franssila S 2012 Oxygen and nitrogen plasma hydrophilization and hydrophobic recovery of polymers *Biomicrofluidics* **6** 016501

[53] Chiolerio A, Rajan K, Roppolo I, Chiappone A, Bocchini S and Perrone D 2016 Silver nanoparticle ink technology: state of the art *Nanotechnol. Sci. Appl.* **9** 1

[54] Nabawy M R A, Parslew B and Crowther W J 2015 Dynamic performance of unimorph piezoelectric bending actuators *Proc. Inst. Mech. Eng.* I **229** 118–29

[55] Wang Q-M and Eric Cross L 1998 Performance analysis of piezoelectric cantilever bending actuators *Ferroelectrics* **215** 187–213